Chapter 2
Fundamentals of Holographic Sensing

Optical devices that reversibly respond to external stimuli can provide fast, quantitative, visual colorimetric readouts in real-time. They may consist of bioactive recognition elements that can transmit the signal through a transducer embedded within the system. Responsive photonic structures may have applications in chemical, biological and physical sensors for medical diagnostics, veterinary screening, environmental monitoring, pharmaceutical bioassays, optomechanical sensing and security applications. This chapter provides an overview of the fabrication of optical devices, and highlights holography as a practical approach for the rapid construction of optical sensors that operate in the visible spectrum and near infrared. It begins with describing the fundamentals of holography and origins of holographic sensors. The chapter also explains the principle of operation of these devices and discusses the design parameters that affect the readouts. The principles of laser light interference during sensor fabrication and photochemical patterning are discussed. Furthermore, computational readout simulations of a generic holographic sensor through a finite element method are demonstrated. Studied design parameters include optical effects due to lattice spacing, nanoparticle (NP) size and concentration, number of stacks, their distribution, and lattice deficiencies within the sensor. Computational simulations allow designing holographic sensors with predictive optical characteristics.

2.1 Fabrication of Optical Devices

Optical devices have been fabricated from photonic band-gap materials [1–6]. These materials function through the periodic modulation of the refractive index in a dielectric medium, which allows filtering out and diffracting narrow-band wavelengths. These optical nanostructures control the propagation of light within dielectric media. Their applications include reflective coatings on lenses, pigments in paints and inks, waveguides, reflective mirrors in laser cavities and optical devices [7–10]. Over the last two decades several top-down and bottom-up fabrication techniques have been developed: Layer-by-layer stacking [11, 12], electrochemical etching [13], laser-beam-scanning chemical vapour deposition [14], and holographic lithography [15]. However, rapidly fabricating structures at

A.K. Yetisen, *Holographic Sensors*, Springer Theses,
DOI 10.1007/978-3-319-13584-7_2

approximately half the wavelength of the visible light remained a challenge [16]. Self-assembly approaches have also been demonstrated, including photonic crystalline colloidal arrays [17–21], block copolymers [22], opals and inverse opals [23] and nanocomposites [24]. Bottom-up approaches involved self-assembly of preformed building blocks such as monodisperse colloidal objects into periodic gratings. Such building blocks may be silica (SiO_2), polystyrene microspheres, or block copolymers. The symmetry, lattice constant of the crystal and the index of refraction contrast can be controlled to fabricate ordered photonic structures. For example, block copolymers self-assemble into periodic regions through phase separation of chemically different polymer blocks [25]. In order to achieve visible-light Bragg diffraction, the diameter of the colloids with ranges from 100 to 1 μm may be used to form one, two and three-dimensional photonic structures [26–28]. Self-assembled photonic structures reduce materials of fabrication and lower costs as compared to nano/microfabricated photonic devices.

Stimulus-responsive materials have been incorporated into these photonic devices to induce a change in their lattice constants or spatial symmetry of the crystalline array, and refractive index contrast. For example, refractive-index tuneable oxide materials such as WO_3, VO_2, and $BaTiO_3$ have been incorporated in these matrices to produce photonic structures that are sensitive to electric field or temperature [29]. The crystalline colloidal arrays infiltrated with liquid crystals optically responded to an applied external electric field and an increase in the temperature of the device [30–32]. Numerous fabrication strategies and materials science have been developed to build responsive photonic structures for applications in sensing chemical stimuli, temperature variation, light, electrical and magnetic fields and mechanical forces [33–40]. However, the challenges included limited tuneability, slow turnaround times and hysteresis. Another critical fabrication issue has been the narrow response range due to the limited external stimuli-induced changes in the lattice spacing or the index of refraction. To overcome these challenges, polymer chemistries, new building blocks and tuning mechanisms evolve to create practical approaches. These methods offer potential feasibility for producing diffraction gratings. However, the control over the material selection, patterning ability, angle of diffraction, three-dimensional organisation of diffracting gratings and rapid manufacturing have been limited. To overcome these limitations, generic fabrication approaches have been developed to improve the capabilities of incorporating 3D images with optical tuneability [18, 21]. An emerging platform among these approaches is holography, which allows fabrication of optical sensors with Bragg gratings for applications in the quantification of chemical, biological and physical stimuli [41].

2.2 History of Holography

Holography allows recording three-dimensional images of an object or digital information through the use of a light-sensitive material and laser light, or micro/nanofabrication techniques [42–46]. In 1865, Maxwell had proposed theoretically

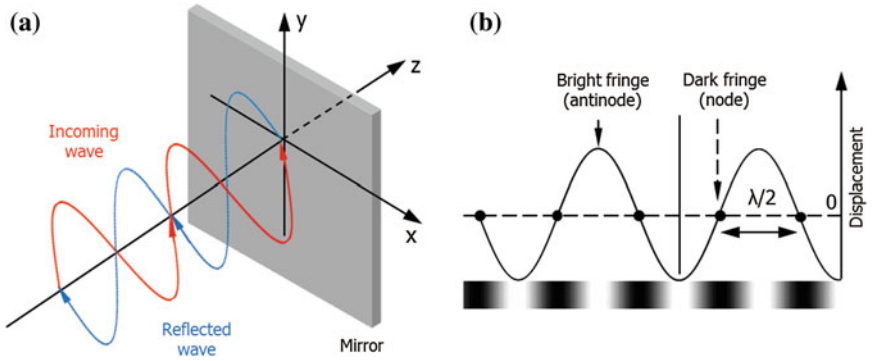

Fig. 2.1 Principle of a standing wave and its corresponding interference pattern. **a** The formation of a standing wave at the plane mirror, **b** Standing wave and interference pattern formed by two coherent beams. Reprinted with permission from [41] Copyright 2014 The American Chemical Society

that light is an electromagnetic disturbance propagating through the field according to electromagnetic laws [47]. In 1869, Zenker theoretically showed that an incident light wave propagating towards a mirror produces a reflected wave, which combines with the incident wave to form an interference pattern with a half-wavelength separation between fringes [48, 49]. In 1887, Hertz experimentally demonstrated the existence of electromagnetic waves by showing that radio waves were consistent with Maxwell's theory [50]. Hertz produced radio standing waves by reflection from a zinc plate. When a monochromatic wave is reflected off a surface, the reflected wave and the incident wave combine to form waves, which oscillate up and down without a direction of motion (Fig. 2.1a). The distance between successive nodes or antinodes is equal to the half of the wavelength of the wave (Fig. 2.1b). Within the standing wave, there is no oscillation at the nodes, while at the antinodes, the oscillations can be maximum.

Zenker's idea to record standing waves of light was experimentally demonstrated by Wiener in the 1890s [51]. He passed carbon arc light, entering a darkroom through a slit, through a prism to filter out the red region of the spectrum. He focused the orthochromatic light using a lens, and directed it perpendicularly to a tilted (2°) 20 nm-thick photographic plate backed by a levelled silver mirror. After he developed and printed the photographic plate, he observed a regular standing wave pattern under magnification. While the antinodes appeared bright, the nodes, containing no light, were dark (Fig. 2.1b). Additionally, the wave might change phase upon reflection, and influence the absolute position of the nodes and antinodes. In 1891, Lippmann developed a method of reproducing colours photographically based on the phenomenon of interference [52]. In his experiment, he projected an image onto a photographic recording medium. The image was produced by shining light through a photographic plate backed by a mirror of liquid mercury, which reflected the light back through the medium to create standing waves. Lippmann was able to create a

latent image (an invisible image before development) produced by the standing waves that are characterised by a series of interference maxima and minima. After the recording medium was developed, fixed and dried through the traditional photographic methods, planes of reduced silver particles had reciprocal distances as a function of the wavelength of the light used during recording. Upon illumination with white light, the silver planes diffracted a coloured projection of the recorded image [53]. In the 1910s, X-ray microscopy for recreating the image from the diffraction pattern of a crystal lattice structure were studied by Bragg, Broersch and Zernike [42, 54]. In the 1920s, Wolfke reported that if an X-ray diffraction pattern is illuminated with a monochromatic light, a new diffraction pattern, which is identical with the image of the object is formed [55]. In the late 1940s, Gabor, while trying to improve the resolution of the electron microscope by overcoming the spherical aberration of the lenses, found that adding a coherent background as a phase reference, the original object wave was contained in an interferogram, which he called a hologram [56, 57]. The term hologram was coined from the Greek words *holos*, meaning "whole," and *gramma*, meaning "message". He received the Nobel Prize in physics in 1971 for establishing the principle of holography. However, the stability of the interference required
(i) mechanical and thermal stability of the interferometer used in the holographic recording, and (ii) a coherent light source.

The foundations of the laser (Light Amplification by Stimulated Emission of Radiation) theory were established in the early years of the 20th century by Einstein [58]. In the 1960s, lasers (optical oscillators) were developed to produce monochromatic light [59, 60]. After the development of the laser, Denisyuk of the former Soviet Union, and Leith and Upatnieks in the US recorded independently the first holograms in 1962 [61, 62]. These early holograms were based on silver halide chemistry. Transmission holograms, originally created by Leith and Upatnieks, require monochromatic light (usually a laser) to view the image, otherwise viewing in white light causes severe chromatic aberrations; whereas holograms produced by Denisyuk's method, can be viewed in light of a broad spectral range [43]. Denisyuk was originally inspired by the method of colour photography constructed by Lippmann. In particular, Denisyuk holograms have generated considerable interest in artistic displays, optical devices, data storage and analytical instruments.

Holographic gratings can be generated using various geometries, which involves the use of multiple collimated laser beams. The first step in recording transmission holograms involves passing a single laser beam through a beam splitter, which divides the beam into two beams. The first beam is expanded by a lens, and deviated by mirrors (front surface) onto an object. The light that is scattered back falls onto a recording medium. Meanwhile the second beam, expanded by a lens, travels directly onto the recording medium. The interference of the two mutually coherent beams forms constructive (antinodes) and destructive (nodes) interferences, at regions of the recording medium dictated by the Fourier transform of the object, which implies that all optical information about the object is coded in the

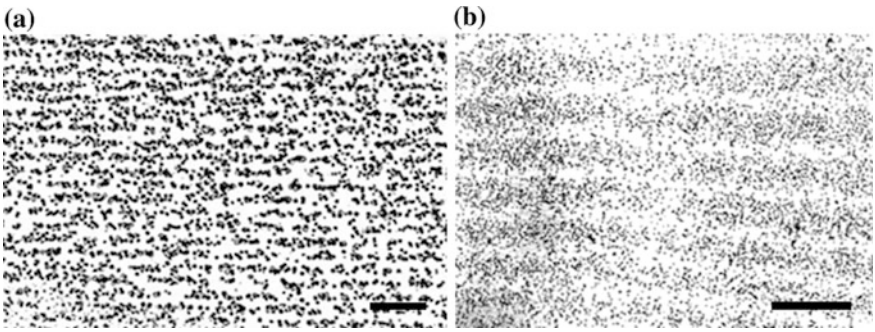

Fig. 2.2 The electron micrographs of hologram cross sections (transversal). **a** A Lippmann phase hologram recorded in a Holotest 8E75HD plate using a HeNe laser operated at 632.8 nm (~50 % diffraction efficiency). Reprinted with permission from [65]. Copyright 1988 The Optical Society of America. **b** A phase hologram recorded in a Slavich PFG-03 M film using a HeNe laser operated at 632.8 nm. *Scale bars* = 1 μm. Reprinted with permission from [41] Copyright 2014 The American Chemical Society

diffraction field produced by the hologram [63]. Holographic recording changes the optical properties of the recording material. An amplitude hologram is recorded when the interference pattern created by the object and the reference beams is copied as variation of the absorption coefficient of the recording material. A phase hologram is created when the holographic recording leads to variation of the refractive index or the thickness of the hologram. Holographic gratings can also be recorded in "Denisyuk" reflection mode. Reflection holograms are typically formed by passing an expanded beam of laser light through the recording plate to illuminate an object on the other side of the plate. Light from the object is then reflected back through the plate and interfered with the light passing through the plate for the first time, thus forming standing waves of light, which are recorded as "holographic fringes" running roughly parallel with the plane of the recording medium [43, 64] (Fig. 2.2). When the hologram is illuminated with a white light source, the fringes in the recording medium act as Bragg mirrors, which diffract light monochromatic (or narrow-band) light and serve as sensitive wavelength filters. The replayed image represents the original object used during the laser exposure. This diffracted light from the periodic gratings results in a narrow-band spectral peak determined by the wavelength of the laser light used and the angle between the two recording beams. The holographic diffraction is governed by Bragg's law:

$$\lambda_{\text{peak}} = 2n_0 \Lambda \sin\theta \tag{2.1}$$

where λ_{peak} is the wavelength of the first order diffracted light at the maximum intensity *in vacuo*, n_0 is the effective index of refraction of the recording medium, Λ is the spacing between the two consecutive recorded NP layers (constant parameter), and θ is the Bragg angle determined by the recording geometry.

2.3 The Origins and Working Principles of Holographic Sensors

In late 1970s, those preparing art holograms realised that so called "pseudo-colour" effects could be obtained by using several exposures of one scene with the 632.8 nm beam from a HeNe laser with each exposure only illuminating different sections of that scene. Before each exposure, the moisture level or pH of the gelatin emulsion was changed, so that each exposure had the emulsion with a different degree of swelling. This resulted in objects having different colours when the finished hologram was replayed under a white light source [66–69]. Specifically, the thickness of the emulsion can be varied through pre-swelling/shrinking the emulsion before laser exposure. Since gelatin film's thickness is greatly affected by its moisture content, moisture control techniques were utilised to create pseudo-colour holograms [68, 70]. In the 1980s, emulsion pre-treatment was optimised to obtain a range of output wavelengths from a fixed exposure wavelength [71, 72]. In the 1990s, the tuning technique of holograms led to the realisation that reflection holograms could be used as sensors to quantify humidity [73] and chemical substances [74–76]. Figure 2.3 shows the timeline in the development of holographic sensors. Any physical or chemical stimulant that changes the lattice spacing (d) or the effective index of refraction (n) of the film cause observable changes in the wavelength (λ_{peak}) or its profile (colour distribution), or the intensity (brightness) of the hologram. The intensity output by the hologram depends on the modulation depth of the refractive index (dark and bright fringes), and the number of planes present in the polymer matrix. Swelling in the polymer matrix increases the distance between NP spacings and produces a red Bragg peak shift, whereas shrinkage in the matrix shifts the peak to shorter wavelengths. The diffraction grating acts as an optical transducer, whose properties are determined by the physical changes in the polymer matrix. For example, when the polymer matrix is functionalised with a receptor comonomer, which has the ability to draw or expel water from the system upon binding, the degree of swelling indirectly represents the concentration of the target analyte. The shift in the Bragg peak can be monitored using a spectrophotometer, and the sensor can be calibrated based on the inputted physical or chemical change. Hence, the same sensor can be optically or visually interpreted to quantify

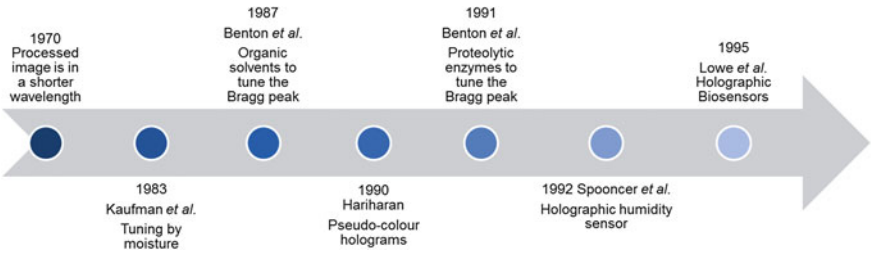

Fig. 2.3 Historical development of holographic sensors

the target analytes in aqueous solutions or physical changes in the environment. This is in contrast to the case of the off-axis transmission hologram, where the holographic fringes run roughly perpendicular to the plane of the plate, and therefore any thickness changes will not greatly shift the Bragg peak. In off-axis transmission gratings, the changes in the brightness or the direction of the diffracted beam can be registered by a photodetector.

Holographic sensors are analytical devices that systematically diffract narrow-band light in the ultraviolet to near-infrared range for application in the detection and quantification of analytes and/or physical parameters [74]. Holographic chemical sensors incorporate gratings within stimuli-responsive polymers, which allow shifting the Bragg peak. Fabrication of the sensors involves laser-directed multi-beam interference and photochemical patterning. The resulting sensors can be interrogated qualitatively by visual inspection or quantitatively by spectrophotometry in real-time. The major advantages of holographic sensors over other optical sensors are the ability to produce three-dimensional (3D) images, control over the angle of off-axis diffraction, and amenability to laser manufacturing. They are functionalised with analyte-responsive materials to construct optical sensors for use in testing, where a visual readout and reversibility are required [77]. Holography allows fabrication of disposable sensors that are lightweight for miniaturisation and multiplexing [78]. Holographic sensors offer three capabilities on a single analytical device: (i) Label-free analyte-responsive polymer, (ii) real-time, reversible quantification of the external stimuli, and (iii) three-dimensional image display. Their applications range from in vitro diagnostics to environmental monitoring (Fig. 2.4).

A holographic sensor can change its optical properties when comes into contact with a target analyte. For example, as a result of detection of an analyte, the sensor could change its spectral response and/or its diffraction efficiency, which in visual terms translates into a change of its colour and/or brightness. The diffraction efficiency of a hologram is described as the ratio of the intensities of the diffracted beam divided by the incident beam. This ratio is a quantitative measure of the brightness of the hologram. Depending on the recording mode and optical properties of the recording media, holograms with controllable optical characteristics can be fabricated. Typical holograms include surface holograms, transmission or reflection holograms, phase or amplitude holograms [79]. For example, "Denisyuk" reflection holograms can be used as colorimetric indicators as they can diffract light when they are illuminated with a white light source. The recording and probing of a reflection hologram is shown in Fig. 2.5a, b. In this recording mode, two coherent beams are incident from the opposite sides of the recording medium. For recording of a "Denisyuk" reflection hologram, two plane waves are normally used, and the lattice spacing of the grating can be determined by Bragg's law (Eq. 2.1).

When the beams have the same incident angles, the interference fringes are parallel to the surface of the recording medium, and an unslanted reflection grating is recorded [80]. The incident angles of the two recording beams can also be different, which produces fringes at an angle with respect to the recording medium surface, and the recorded grating will be slanted. In either case, the fringes run along the bisector line of the angle between the two beams. The optical

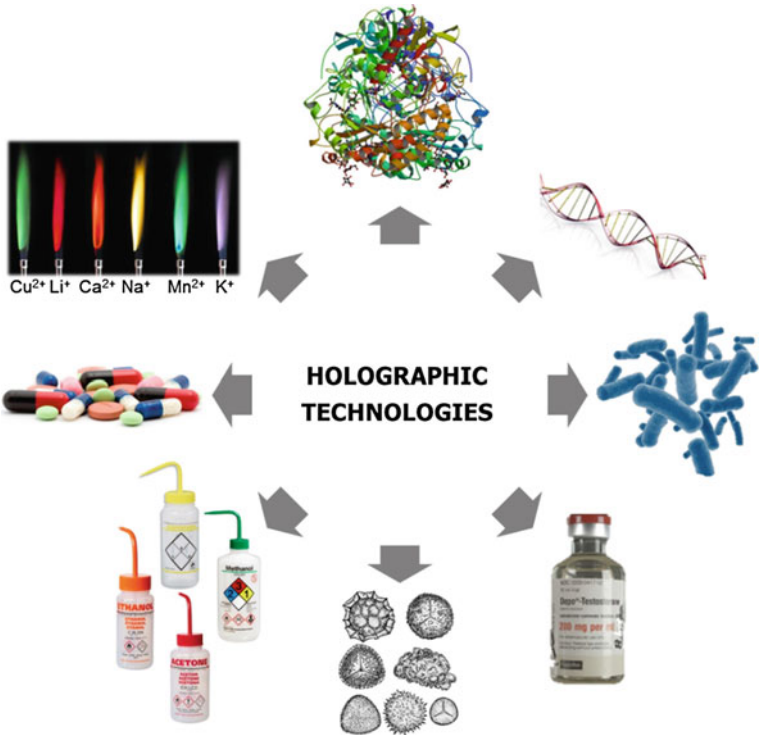

Fig. 2.4 The applications of holographic sensors in medical diagnostics and environmental testing

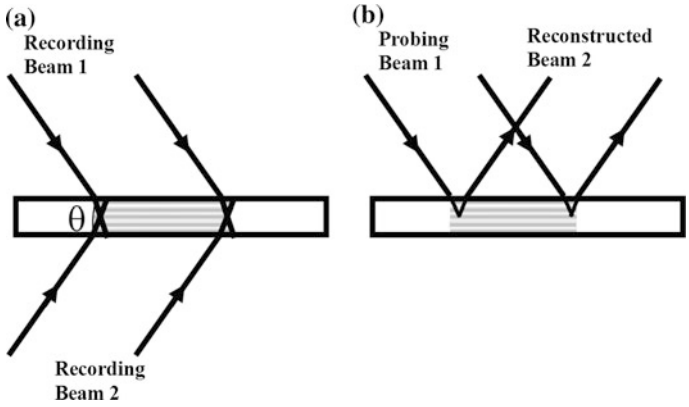

Fig. 2.5 Denisyuk reflection holograms.**a** Recording and **b** probing the hologram. Reprinted with permission from [41] Copyright 2014 The American Chemical Society

characteristic that most conveniently can be observed to change in reflection holograms in the presence of an analyte is the wavelength of the diffracted light. When illuminated with light of a broad spectral range, a reflection hologram diffracts selectively, and operates as a wavelength filter. The maximum diffraction efficiency occurs at a wavelength that satisfies Eq. (2.1). A change in either of the effective refractive index or the lattice spacing causes a change in the wavelength of the diffracted light (Eq. 2.1). It is assumed that the hologram has a thick volume and the angle of observation is constant. In order to quantify how different parameters influence the Bragg peak position, we differentiate Eq. (1.1) using the product rule:

$$\Delta\Lambda = 2\Delta n_0 \Lambda \sin\,\theta + 2n_0 \Delta\Lambda \sin\,\theta + 2n_0 \Lambda \cos\,\theta\,\Delta\theta \tag{2.2}$$

where $\Delta\lambda$, Δn_0, $\Delta\Lambda$ and $\Delta\theta$ are the changes in the position of the Bragg peak, effective index of refraction, grating period and the Bragg angle, respectively. We divide both sides of Eq. (2.2) by $2n_0\Lambda \sin\theta$:

$$\frac{\Delta\lambda}{2n_0\Lambda\,\sin\,\theta} = \frac{2\Delta n_0 \Lambda\,\sin\,\theta}{2n_0\Lambda\,\sin\,\theta} + \frac{2n_0\Delta\Lambda\,\sin\,\theta}{2n_0\Lambda\,\sin\,\theta} + \frac{2n_0\Lambda\,\cos\,\theta\Delta\theta}{2n_0\Lambda\,\sin\,\theta} \tag{2.3}$$

which can be simplified as:

$$\frac{\Delta\lambda}{\lambda} = \frac{\Delta n_0}{n_0} + \frac{\Delta\Lambda}{\Lambda} + \frac{\cos\theta\Delta\theta}{\sin\theta} \tag{2.4}$$

$$\frac{\Delta\lambda}{\lambda} = \frac{\Delta n_0}{n_0} + \frac{\Delta\Lambda}{\Lambda} + \cot\theta\Delta\theta \tag{2.5}$$

Using Eq. (2.5), the influence of the changes of optical properties on the Bragg peak can be modelled. Any dimensional change of the polymer matrix in which the hologram is recorded, such as swelling or shrinking produces a change in the lattice spacing, and thus alters the spectral response of the hologram (Fig. 2.6a). A typical Bragg peak shift of a holographic sensor is shown in Fig. 2.6b, and the shift as a function of analyte concentration (Fig. 2.6c). A simulation assuming that the effective refractive index and probe angle remain constant reveals that practically achievable changes in the volume of the polymer matrix could produce large changes in the wavelength of the Bragg peak (Fig. 2.6d). A dimensional change of 30 %, which is normally achieved in an acrylamide-based photopolymer hologram, would produce over a 100 nm shift depending on the initial Bragg peak wavelength [80].

The effective refractive index of the polymer matrix in which the hologram is recorded can change due to the absorption of the target analyte. Assuming that the only property that changes the effective refractive index, the resulting change in the Bragg peak wavelength can be calculated using Eq. (2.5) (Fig. 2.6e). The initial effective refractive index was 1.5. A significant change in the effective refractive index is required in order to obtain a visually observable change in the peak wavelength (Fig. 2.6e). For example, an effective refractive index change of

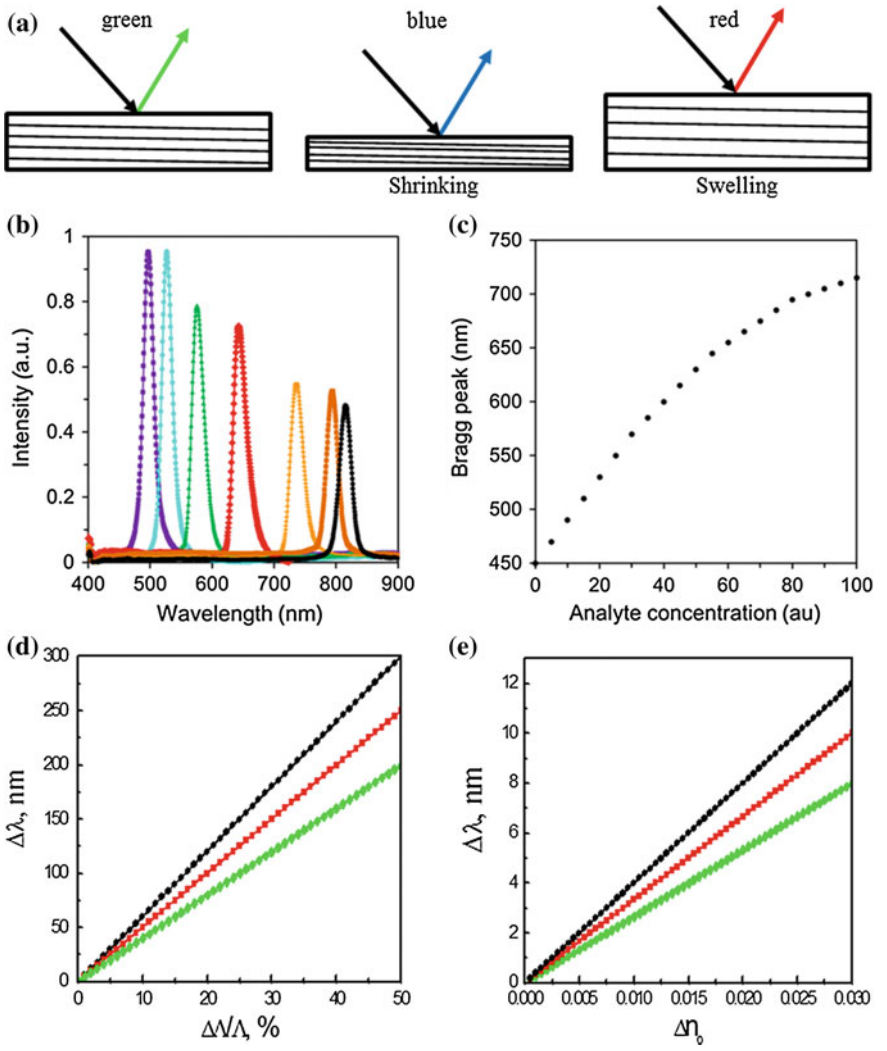

Fig. 2.6 Principle of operation of a Denisyuk reflection holographic sensor. **a** A dimensional change, shrinkage or swelling of the polymer matrix, produces a change in the grating period and a change in the position of the Bragg peak. **b** A typical spectra as the concentration of the analyte changes, **c** The shift in the Bragg peak, **d** Simulated Bragg peak shift as a function of change in lattice spacing. Assuming that the effective refractive index and the Bragg angle (θ) remain constant, as the relative dimensional change (ΔΛ/Λ) increases, the Bragg peak shifts to longer wavelengths. Practically achievable changes in lattice spacing can produce Bragg shifts larger than 300 nm. The initial Bragg peaks are 600 (●), 500 (■), 400 nm (♦). **e** Bragg peak shift as a function of change in refractive index. Assuming that the initial effective refractive index (n_0) is 1.5 and the Bragg angle (θ) remain constant, as the effective refractive index increases, the Bragg peak shifts to longer wavelengths. Practically achievable changes in refractive index can produce Bragg shifts up to ~12 nm. The initial Bragg peaks are 600 (●), 500 (■), 400 nm (♦). Reprinted with permission from [41] Copyright 2014 The American Chemical Society

15×10^{-3} produces a ~6 nm Bragg peak shift for a sensor originally operating at 600 nm [80]. With the grating period and probe angle remaining constant, it is preferable to record the hologram at a longer wavelength. The absolute change in the peak wavelength ($\Delta\lambda$) can be increased by choosing materials with lower initial effective refractive index (n). Materials with higher porosity have lower effective refractive index. Moreover, for the detection of larger size analytes, it is preferable to use recording media with larger pore size, which allow the diffusion of the analyte into the polymer matrix easily. Both the dimensional and the effective refractive index effects contribute simultaneously to the change in the spectral response of the hologram. For example, in gelatin-based sensors the effective refractive index decreases as the sensor absorbs water and swells; thus, the two factors have opposite contributions to the spectral shift. However, in some materials, one of the factors is the main contributor. For example, in humidity sensors recorded in acrylamide-based photopolymer, the main contributor is the swelling of the polymer matrix due to absorption of moisture studied at relative humidity up to 80 % [81].

2.4 Computational Modelling of Holographic Sensors in Fabrication and Readout

The principles of laser light interference in the fabrication of responsive diffraction gratings are discussed. This chapter is divided into two parts; while the first part explains the photochemical patterning during recording of holographic sensors in Denisyuk reflection mode, the second part describes the operation of the sensors. The first part focuses on the fundamentals of the laser writing in which materials get physically broken, displaced or removed by means of optical forces and thermal energy. In order to understand the different phenomena during photochemical patterning, interference patterns during laser light exposure were simulated. The second part of this chapter demonstrates computational simulations of a generic holographic sensor through a finite element model [82, 83]. To design the sensors with predictive characteristics, its optical properties due to variation in the pattern and the characteristics of the NP arrays were evaluated. Various factors including NP size and distribution within the polymer matrices that directly affect the performance of the sensors were studied computationally.

2.4.1 Photochemical Patterning

In order to predict the interference patterns, which produce the photonic structure in Denisyuk reflection mode, the system was modelled during fabrication as arising from a superposition of different light waves [84–87]. Figure 2.7a shows a schematic of the experimental setup during laser light exposure. Simplifying the simulation of

photochemical patterning, the interference pattern created was evaluated from three waves: (1) incident beam (λ_1), (2) beam reflected from the mirror (λ_2), (3) beam reflected internally at the hydrogel-water interface (λ_3). There is a fourth beam that may also be reflected from the mirror, however, this beam was neglected to simplify the simulation. The intensity distribution of the field along the hydrogel was reconstructed by simulating the interference of the three plane waves. Through computing the respective intensities and phases of individual plane waves, the resulting interference pattern was extracted. To visualise the intensity distribution in a 2D cross-section plane, the electromagnetic field in every point over an area of $10 \times 10\ \mu m^2$ inside the hydrogel was evaluated. Figure 2.7b shows the interference pattern of the three distinct plane waves, taking into account: the tilt angle, effective index of refraction, laser light wavelength, and exponential decay of laser light intensity while the laser light travels through the hydrogel-Ag^0 NP system and the laser light phase changes upon reflection from the mirror. In order to simulate the laser-induced photochemical patterning, it was assumed that the energy of a single pulse (6 ns, 240 mJ) gets transmitted instantaneously to the particles before heat diffusion is involved. Investigated conditions included materials with considerably thicker than the wavelength of the laser light. Notably, the localisation of heat along the standing wave might be required to produce a well-defined photonic structure. The model was simplified by implying that photochemical patterning occurs, where the energy concentration exceeds a given threshold. Figure 2.7c shows the simulation of the structure after photochemical patterning. In the simulated pattern, black regions correspond to the non-patterned material, while white regions represent photochemically patterned material. Along with the vertical standing wave ($\sim$193 nm), a larger period wave ($\sim$3 μm) is in the horizontal direction. Thus, using

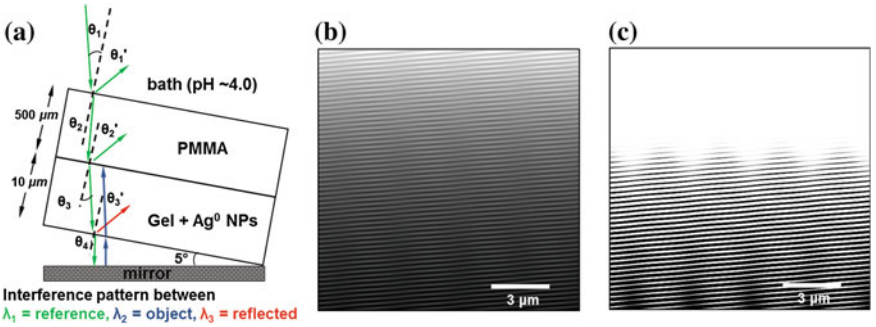

Fig. 2.7 Photochemical patterning based on multi-beam interference in Denisyuk reflection mode. **a** Schematic of the laser light-induced photochemical patterning setup for the preparation of holographic sensors. **b** Intensity field distribution obtained from a holographic sensor with a tilting angle of 5°. The image corresponds to the intensity distribution $I = |E|^2$ produced by laser light interference inside the hydrogel, created by three beams: (1) incident beam, (2) beam reflected from the mirror and (3) beam reflected internally at the pHEMA-water interface. **c** Threshold of intensity of the cross section to represent patterned and nonpatterned regions. The period of the surface grating is 3.01 μm. Reprinted with permission from [84] Copyright 2014 Wiley-VCH Verlag GmbH&Co. KGaA, Weinheim

simulation, we can predict the optical characteristics such as the periodicity of the transmission grating, regions that will be patterned at a given transmission or absorption values and the number of multilayer gratings that will be formed during fabrication.

2.4.2 Simulations of the Optical Readouts

The operation of the holographic sensor is governed by the periodicity of its lattice spacing, which controls the propagation of light through the structure. The lattice periodicity consists of an alternating pattern of mesoscale Ag^0 NP regions organised in a specific direction within a hydrogel [88, 89]. If the absorption of light by the entire structure is minimum and a contrast is present between the periodic Ag^0 NP regions, some frequencies are filtered out as they pass through the photonic structure. The excluded group of frequencies is called the photonic band gap (PBG). The dynamic coloration is generally obtained by altering the periodicity of nanoparticle regions either by changing the lattice spacing or the refractive index of the multilayers through chemical reactions. Dynamic coloration in nature include fish (e.g. *Paracheirodon innesi*) [90, 91], cephalopods (e.g. *Euprymna scolopes*) [92] and beetles (e.g. *Tmesisternus isabellae*) [93]. Holographic sensors are analogous to these structures, where the frequency range is designed for a specific PBG. For example, for infrared frequencies, micron dimensions are required for the geometry of the structure [94]. In holographic sensors, the Ag^0 NP-based multilayer structure that was formed within the hydrogel acts as a dynamic 1D photonic crystal, which diffracts the frequencies of electromagnetic radiation that fall within the band gap region. When the band gap region shifts its position to higher or lower frequencies by changing the geometry of the hydrogel, different frequencies are back scattered. To present the principle of operation and provide evidence for subsequent optimisation of a holographic sensor, a finite element method based on computational software COMSOL Multiphysics®, was utilised [82, 83, 95]. The theoretical diffraction grating consisted of periodic layers of Ag^0 NPs in a hydrogel matrix. The diffraction grating patterns consisting of stacks of randomly-sized Ag^0 NPs were generated using a MATLAB® code. Since the hydrogel matrix has a refractive index close to that of water, and the laser wavelength used for the photochemical patterning was λ = 532 nm, according to Bragg's law, $\lambda/2n$ results in a lattice constant of l = 176 nm. The 1D periodic array of stacks consisted of Ag^0 NPs, which were designed as nanospheres with different radii (Fig. 2.8a).

The simulated geometry consisted of 6 stacks with ~60 Ag^0 NPs per stack. Along the vertical axis of each stack, the Ag^0 NPs were uniformly distributed, whilst in the horizontal axis, the Ag^0 NPs were distributed within the layers defined by the laser-induced photochemical patterning. To achieve this, a normal random distribution was performed with the mean positions of the stacks set to a distance equal to the lattice constant. Additionally, to obtain a realistic photonic structure in terms of representing a holographic sensor, a normal random distribution was also

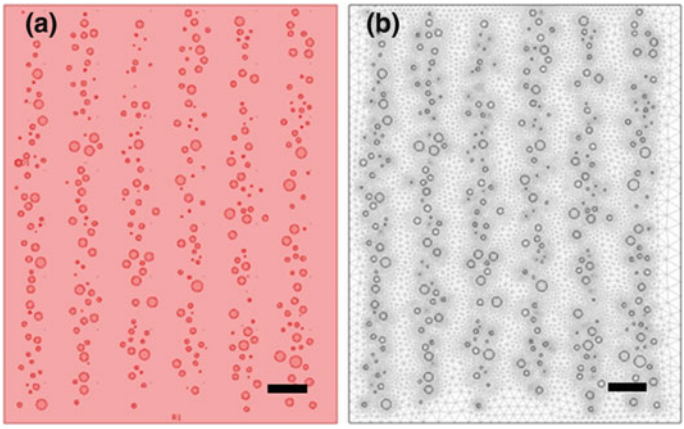

Fig. 2.8 A simulated geometry of a holographic sensor with a multilayer grating. **a** Organisation of Ag^0 NP stacks within a hydrogel matrix, **b** Forming a geometric mesh of the Ag^0 NP pattern. *Scale bars* = 150 nm. Reproduced from [83] with permission from The Royal Society of Chemistry

used to define the radii of the Ag^0 NPs. The mean value of the radii was set to 4–24 nm with σ = 5 nm. After generating the Ag^0 NP patterns in MATLAB®, they were imported into COMSOL Multiphysics® for modelling. The pattern of Ag^0 NP was surrounded with a square domain of a medium that is analogous to a hydrogel matrix. The remaining Ag^0 NP subdomains were set to have an electrical conductivity of Ag^0 (61.6 mS/m). Since Ag^0 NPs absorbs electromagnetic radiation, a complex refractive index was required. This absorption does not significantly affect the propagation of light when a small number of stacks are simulated. However, the absorption can reduce the efficiency of diffracted light in a holographic sensor that have a high number of Ag^0 NP stacks. Figure 2.8b illustrates the geometric mesh of the holographic sensor in COMSOL Multiphysics®. The incident electromagnetic waves were propagated from left to right along the array of Ag^0 NP stacks. The left boundary of the cell was set to a scattering boundary condition. The light source was defined as a plane wave of varying wavelengths [95]:

$$n \times (\nabla \times H_z) - jkH_z = -jk(1 - k \cdot n)H_{oz} \exp(-jkr) \tag{2.6}$$

where n is the complex refractive index, H_z is the magnetic field strength at position r, k is the propagation constant, and H_{oz} is the initial magnetic field strength. Meshing was performed with a finite element size of ∼2 nm to resolve each Ag^0 NP. Once meshing was established, a computation was performed via a parametric sweep, which allowed solving for a range of wavelengths. The wavelength parameters set covered 400–900 nm. Finally, using "power outflow and time average" boundary integration, the transmitted waves were collected at the opposite side of the holographic sensor. Figure 2.9a–c illustrates the simulated geometry that resembles the configuration of a typical holographic sensor, and Fig. 2.9d shows the

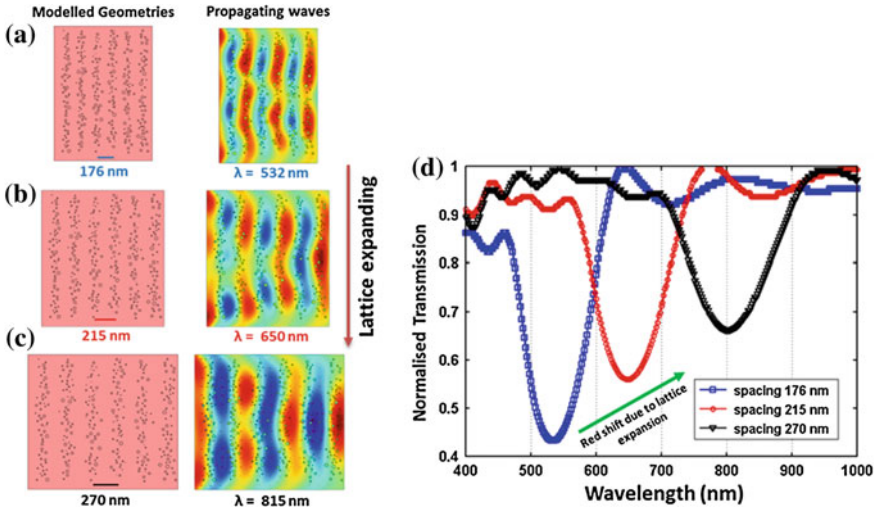

Fig. 2.9 Simulated geometries and transmission spectra for the holographic sensors with lattice constants of **a** 176, **b** 215 and **c** 270 nm. **d** The transmission spectra as a function of lattice spacing. Reproduced from Ref. [83] with permission from The Royal Society of Chemistry

transmission spectra. The spectrum for 176 nm lattice spacing showed peak reflectivity at ~532 nm that underwent the lowest transmission due to Bragg diffraction, which defined the diffracted green colour of the holographic sensor (Fig. 2.9a). The colour of the holographic sensor was dictated by the spacing between the Ag^0 NP stacks. The effect of expanding the Ag^0 NP lattice on the reflection band gaps was analysed. The multilayer structure was expanded, while keeping the density and diameter of the Ag^0 NPs constant, simulating the operation of a holographic sensor. The lateral expansion of the polymer matrix increased the effective-stack spacing and stack size, and it reduced the concentration of Ag^0 NPs per stack (Fig. 2.9a–c). The overall effect of these changes on the wave propagation was observed in the simulated transmission spectra, which showed a shift to longer wavelengths in the reflection bands as the Ag^0 NP stack spacing was increased (Fig. 2.9d). The expanding sensor displayed a colour change (reflection band) across the visible spectrum from ~532 to 800 nm. As the Ag^0 NP stack spacing increases, the reflection efficiency (intensity) of the sensor decreases. This may be attributed to the decrease in the concentration of Ag^0 NPs present in each stack, which reduces the contrast of the effective refractive index between the Ag^0 NP stacks and the surrounding hydrogel matrix.

The effect of varying Ag^0 NP radii on the efficiency of the holographic sensor was evaluated. Nine different geometries were generated with mean Ag^0 NP radii from 6 to 22 nm, while the number of Ag^0 NPs per stack was kept constant at 60. The transmission spectra showed that as the radii of Ag^0 NPs increased, the intensity of the reflection band also increased, which could be attributed to the area that these respective Ag^0 NPs spread (Fig. 2.10). An increase in the contrast of the

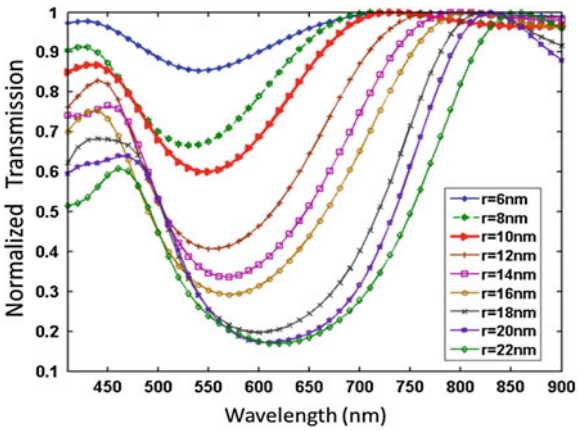

Fig. 2.10 Simulated transmission spectra for the holographic sensors with Ag^0 NPs at different mean radius at a lattice constant of 176 nm with 60 Ag^0 NPs per stack

effective index of refraction of the Ag^0 NP stacks increased the reflection. Therefore, if all these configurations have the same number of Ag^0 NPs, larger Ag^0 NPs would cover more area within the hydrogel matrix, thus resulting in a higher effective index of refraction. However, a photonic structure with Ag^0 NPs larger than ø 100 nm would induce a broad bandwidth and a redshift on the reflection band gap [96]. The broad bandwidth can be explained by the uneven uniformity in the width of the stacks in a holographic sensor. For example, for $r = 22$ nm, not all the five stacks had the same width, because MATLAB® attempted to generate a pattern, where the Ag^0 NPs were evenly spaced inside a stack, and hence it placed them along the horizontal direction. The reflection band shift to longer wavelengths can be explained by the surface plasmonic resonances of the Ag^0 NP [97]. The excitation of surface plasmons arises from a collective electron oscillation within the nanostructure induced by the incident light. This leads to an optical local-field enhancement and a dramatic wavelength-selective photon scattering localised at nanoscale. The plasmonic resonances were affected by the Ag^0 NP radii and geometry, and the optical properties of hydrogel matrix. The reflected light/band gaps displayed by a holographic sensor were influenced by the plasmonic resonances of the Ag^0 NPs. As the radii of the Ag^0 NPs increased, the peak plasmonic resonance shifted to longer wavelengths. Therefore, the band gaps broadened as they represent an effective reflection due to the periodicity of the stacks and the surface plasmon resonances of the larger Ag^0 NPs. The ideal Ag^0 NP radius is between 8 and 10 nm even if they produce weaker reflections than the NP with larger radii. In this radius range, the surface plasmon resonance and the lattice constant dictated band gaps coincide. The reflection efficiency can also be improved by increasing the concentration of the Ag^0 NPs.

The effect of changing the number of Ag^0 NP stacks on the efficiency of the holographic sensor was studied. Three configurations consisting of 60 Ag^0 NPs per stack with a mean radius of 10 nm and a lattice constant of 182 nm were simulated (Fig. 2.11a–c), and their transmission spectra were extracted (Fig. 2.11d).

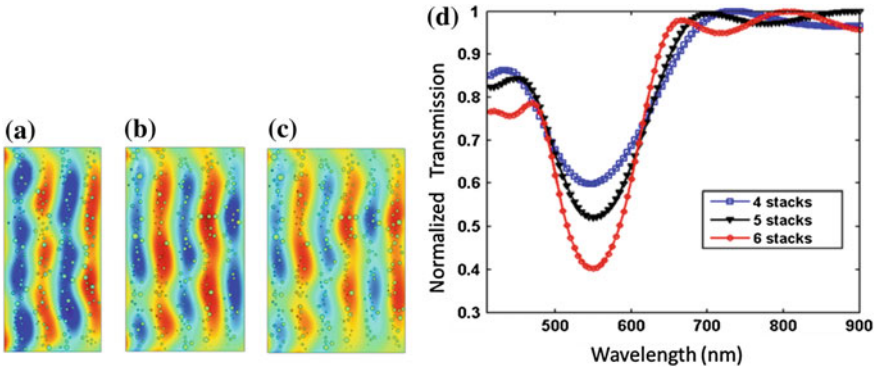

Fig. 2.11 Simulated transmission spectra for the holographic sensors as a function of the number of Ag^0 NP stacks. **a** 4, **b** 5 and **c** 6 stacks of Ag^0 NPs with a lattice constant of 182 nm. **d** The wave propagation spectra for the transmission along the photonic structure with 4, 5 and 5 Ag^0 NP stacks. Stop band is centred at ~550 nm. Reproduced from [83] with permission from The Royal Society of Chemistry

The position of the reflection band was at 550 nm, and it did not change by adding or removing stacks of Ag^0 NP with the same periodicity. As the number of Ag^0 NP stacks increased, the intensity of the reflected light also increased. For 6, 5, 4 stacks, 60, 48 and 40 % reflection was obtained. At 6 stacks the reflection was stronger than configurations with fewer stacks. Additionally, the lower the reflection, the wider the trough was. The width at half maximum (FWHM) of the 4 stack curve was 160 nm, whereas 6 stacks had 110 nm. Consequently, the greater the number of Ag^0 NP stacks, the deeper the PBG trough and the narrower the bandwidth was.

The concentration of Ag^0 NPs of the holographic sensors was varied from 20 to 80 Ag^0 NPs per stack (Fig. 2.12a–d). Comparing the geometries of the models, as the number of Ag^0 NPs per stack increased, the stacks became more uniform; resembling a continuous medium with fewer voids. Hence, the effective index of refraction of the stacks differed in each case. 20 Ag^0 NPs per stack produced a weak reflection (Fig. 2.12e). With an increasing number of Ag^0 NPs per stack, the reflection band became stronger, with the deepest one reaching 65 % of reflection for 80 Ag^0 NPs per stack. Increasing the number of Ag^0 NP increased the contrast of the index of refraction, thus resulting in higher diffraction efficiencies. However, as the density of Ag^0 NPs per stack increased, the net absorption also increased, leading to effectively lower transmission. The position of the trough shifted to longer wavelengths when the concentration of Ag^0 NPs per stack increased. At 20 Ag^0 NPs per stack, the dip of the curve was located at ~530 nm, but for 40–60 Ag^0 NPs per stack, the dip was located at ~555 nm. This shift could be due to a shift in the surface plasmon resonance caused by the close proximity of Ag^0 NPs, and the overall increase in the size of the stacks [96]. Therefore, an increase in the Ag^0 NP concentration per stack resulted in an increase in the refractive index contrast of the holographic sensors.

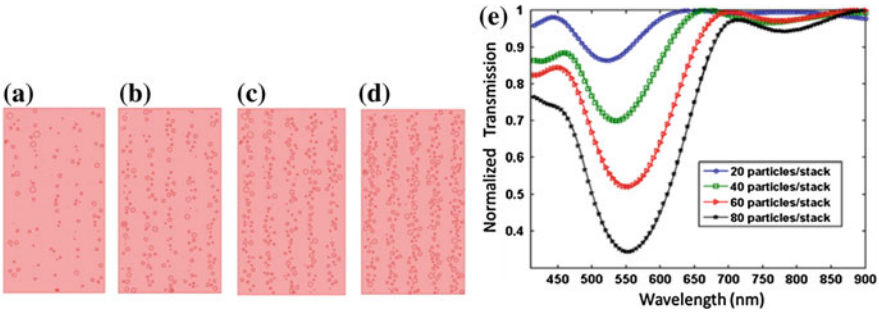

Fig. 2.12 Simulated geometry and the transmission spectra of the holographic sensor as the number of Ag^0 NP stacks was varied. **a** 20, **b** 40, **c** 60 and **d** 80 Ag^0 NPs per stack. **e** The transmission spectra for 20–80 Ag^0 NP per stack. Reproduced from Ref. [83] with permission from The Royal Society of Chemistry

Inhomogeneous Ag^0 NP distribution through the hydrogel matrix may affect the optical properties of the sensor. The effect of anomalies in the holographic sensor was evaluated by simulating four configurations, in which the mean radii of the Ag^0 NPs differed (Fig. 2.13). Distortions are normally present in laser-directed fabrication of holograms, since the Ag^0 NPs are introduced into the polymeric matrices through a diffusion and photographic development, leading to inhomogeneous distribution of NP regions within the hydrogel matrix [98]. The simulated geometries contained six stacks, and they all began with the first stack of Ag^0 NP mean radius of 10 nm. Figure 2.13a–d shows the configurations with Ag^0 NP mean radius that increased by 0.5 nm per stack from 10 to 12 nm. The simulations allowed evaluation of errors due to uncontrolled Ag^0 NP during holographic sensor fabrication. The transmission spectra in Fig. 2.13e show a reference curve for which there is a constant mean radius along all the stacks with the remaining curves representing

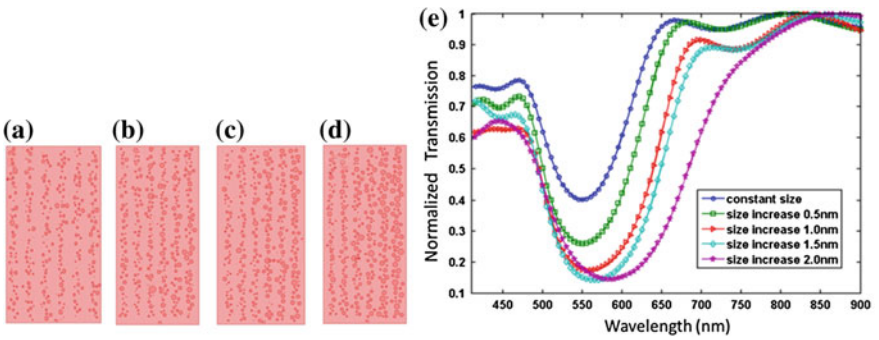

Fig. 2.13 Simulated transmission spectra of the holographic sensor as a function of increasing Ag^0 NP mean radius. Starting from 10 nm, the Ag^0 NP mean radius was increased by **a** 0.5, **b** 1.0, **c** 1.5 and **d** 2.0 nm per stack. **e** Transmission spectra of these configurations as compared to a pattern with constant mean radii. Reproduced from [83] with permission from The Royal Society of Chemistry

a change of mean radius size. In the worst-case scenario of an increase of 2 nm per stack, the curve shows a trough being wider and centred at ~585 nm rather than 550 nm. The lattice constant of the reference curve differs from the worst-case scenario, as the latter has a smaller effective lattice constant. In Fig. 2.13d, the distance between the last two stacks is small, hence, the overall effective lattice constant is smaller. Additionally, the spacing between each pair of stacks is non-uniform, which leads to band gap overlaps, which effectively produce a wide bandwidth. This may result in a stronger reflection from the holographic sensor, but poor selectivity (broadband response) for an optical device that needs to exhibit narrow-band peak.

2.5 Conclusions

This chapter described computational modelling of photochemical patterning of recording media in Denisyuk reflection mode, and provided simulations to study the parameters that affect the efficiency of the sensors during readouts. In the first section, grating formation was studied. A threshold of laser light intensity must be passed in order to photochemically pattern the recording media and form a diffraction grating. The produced grating should be produced at the lowest tilt angle to reduce the effect of transmission grating, which broadens the Bragg peak in the readouts. In order to reduce the transmission grating, decane (RI: 1.41) can be used as an index matching fluid during laser exposure, and this inert and odorless compound does not react with hydrogel matrices. In the second part, a photonic multilayer structure based on a stack of Ag^0 NP layers within a hydrogel was computationally studied, and different parameters affecting its performance were evaluated. An optical photonic multilayer structure based on a stack of Ag^0 NP layers within a hydrogel-based system (1D photonic structure) was computationally studied and different parameters affecting its performance were evaluated. The degree of Bragg diffraction and bandwidth of the holographic sensor can be controlled for a desired range by modifying the geometry and distribution of the Ag^0 NP within the hydrogel matrix. The intensity of the reflection band increases as the number of Ag^0 NP stacks increases. The reflection intensity dramatically increases, along with a narrowing of the bandwidth, even by the addition of two extra Ag^0 NP stacks. An increase in the number of Ag^0 NPs is proportional to both the depth and width of the bandwidth. The fabrication of holographic sensors by laser light allows formation of gratings with controlled diffraction angle and pattern [84]. The model demonstrated in this chapter can also be utilised to simulate other nanostructures [99–101]. This theoretical approach allows designing holographic sensors with predictive optical properties, which might reduce the barriers in their integration with point-of-care diagnostic devices [102–105], microfluidic assays [106], contact lens sensors [107] and smartphones [108, 109]. By rationally fabricating

holographic sensors with high control over the entire system, including the size and distribution of the Ag^0 NPs within hydrogel matrices, one can avoid undesirable effects such as red-shifted diffraction and wider band gaps.

References

1. Aoki K, Guimard D, Nishioka M, Nomura M, Iwamoto S, Arakawa Y (2008) Coupling of quantum-dot light emission with a three-dimensional photonic-crystal nanocavity. Nat Photonics 2(11):688–692. doi:10.1038/nphoton.2008.202
2. Rinne SA, Garcia-Santamaria F, Braun PV (2008) Embedded cavities and waveguides in three-dimensional silicon photonic crystals. Nat Photonics 2(1):52–56. doi:10.1038/nphoton.2007.252
3. Takahashi S, Suzuki K, Okano M, Imada M, Nakamori T, Ota Y, Ishizaki K, Noda S (2009) Direct creation of three-dimensional photonic crystals by a top-down approach. Nat Mater 8 (9):721–725. doi:10.1038/nmat2507
4. Ishizaki K, Noda S (2009) Manipulation of photons at the surface of three-dimensional photonic crystals. Nature 460(7253):367–370. doi:10.1038/nature08190
5. Llordes A, Garcia G, Gazquez J, Milliron DJ (2013) Tunable near-infrared and visible-light transmittance in nanocrystal-in-glass composites. Nature 500(7462):323–326. doi:10.1038/nature12398
6. Kolle M, Lethbridge A, Kreysing M, Baumberg JJ, Aizenberg J, Vukusic P (2013) Bio-inspired band-gap tunable elastic optical multilayer fibers. Adv Mater 25(15):2239–2245. doi:10.1002/adma.201203529
7. Yablonovitch E (2001) Photonic crystals: semiconductors of light. Sci Am 285(6):47–51, 54–45
8. Krauss TF (2003) Photonic crystals—cavities without leaks. Nat Mater 2(12):777–778. doi:10.1038/Nmat1026
9. Akahane Y, Asano T, Song BS, Noda S (2003) High-Q photonic nanocavity in a two-dimensional photonic crystal. Nature 425(6961):944–947. doi:10.1038/nature02063
10. Norris DJ (2007) Photonic crystals. A view of the future. Nat Mater 6(3):177–178. doi:10.1038/nmat1844
11. Lin SY, Fleming JG, Hetherington DL, Smith BK, Biswas R, Ho KM, Sigalas MM, Zubrzycki W, Kurtz SR, Bur J (1998) A three-dimensional photonic crystal operating at infrared wavelengths. Nature 394(6690):251–253. doi:10.1038/28343
12. Noda S, Tomoda K, Yamamoto N, Chutinan A (2000) Full three-dimensional photonic bandgap crystals at near-infrared wavelengths. Science 289(5479):604–606. doi:10.1126/science.289.5479.604
13. Birner A, Wehrspohn RB, Gosele UM, Busch K (2001) Silicon-based photonic crystals. Adv Mater 13(6):377–388. doi:10.1002/1521-4095(200103)13:6<377:Aid-Adma377>3.0.Co;2-X
14. Wanke MC, Lehmann O, Muller K, Wen Q, Stuke M (1997) Laser rapid prototyping of photonic band-gap microstructures. Science 275(5304):1284–1286. doi:10.1126/science.275.5304.1284
15. Campbell M, Sharp DN, Harrison MT, Denning RG, Turberfield AJ (2000) Fabrication of photonic crystals for the visible spectrum by holographic lithography. Nature 404 (6773):53–56. doi:10.1038/35003523
16. Xia YN, Gates B, Yin YD, Lu Y (2000) Monodispersed colloidal spheres: old materials with new applications. Adv Mater 12(10):693–713. doi:10.1002/(Sici)1521-4095(200005)12:10<693:Aid-Adma693>3.0.Co;2-J
17. Zhao YJ, Zhao XW, Gu ZZ (2010) Photonic crystals in bioassays. Adv Funct Mater 20 (18):2970–2988. doi:10.1002/adfm.201000098

18. Ge J, Yin Y (2011) Responsive photonic crystals. Angew Chem Int Ed 50(7):1492–1522. doi:10.1002/anie.200907091
19. Galisteo-Lopez JF, Ibisate M, Sapienza R, Froufe-Perez LS, Blanco A, Lopez C (2011) Self-assembled photonic structures. Adv Mater 23(1):30–69. doi:10.1002/adma.201000356
20. Buenger D, Topuz F, Groll J (2012) Hydrogels in sensing applications. Prog Polym Sci 37 (12):1678–1719. doi:10.1016/j.progpolymsci.2012.09.001
21. Zhao Y, Xie Z, Gu H, Zhu C, Gu Z (2012) Bio-inspired variable structural color materials. Chem Soc Rev 41(8):3297–3317. doi:10.1039/c2cs15267c
22. Schacher FH, Rupar PA, Manners I (2012) Functional block copolymers: nanostructured materials with emerging applications. Angew Chem Int Ed 51(32):7898–7921. doi:10.1002/anie.201200310
23. Aguirre CI, Reguera E, Stein A (2010) Tunable colors in opals and inverse opal photonic crystals. Adv Funct Mater 20(16):2565–2578. doi:10.1002/adfm.201000143
24. Bonifacio LD, Lotsch BV, Puzzo DP, Scotognella F, Ozin GA (2009) Stacking the nanochemistry deck: structural and compositional diversity in one-dimensional photonic crystals. Adv Mater 21(16):1641–1646. doi:10.1002/adma.200802348
25. Urbas A, Fink Y, Thomas EL (1999) One-dimensionally periodic dielectric reflectors from self-assembled block copolymer-homopolymer blends. Macromolecules 32(14):4748–4750. doi:10.1021/Ma9903207
26. Matsushita SI, Yagi Y, Miwa T, Tryk DA, Koda T, Fujishima A (2000) Light propagation in composite two-dimensional arrays of polystyrene spherical particles. Langmuir 16 (2):636–642. doi:10.1021/La990676b
27. Rogach A, Susha A, Caruso F, Sukhorukov G, Kornowski A, Kershaw S, Mohwald H, Eychmuller A, Weller H (2000) Nano- and microengineering: Three-dimensional colloidal photonic crystals prepared from submicrometer-sized polystyrene latex spheres pre-coated with luminescent polyelectrolyte/nanocrystal shells. Adv Mater 12(5):333–337. doi:10.1002/(Sici)1521-4095(200003)12:5<333:Aid-Adma333>3.0.Co;2-X
28. Yin YD, Lu Y, Xia YN (2001) Assembly of monodispersed spherical colloids into one-dimensional aggregates characterized by well-controlled structures and lengths. J Mater Chem 11(4):987–989. doi:10.1039/B009606g
29. Zhou J, Sun CQ, Pita K, Lam YL, Zhou Y, Ng SL, Kam CH, Li LT, Gui ZL (2001) Thermally tuning of the photonic band gap of SiO_2 colloid-crystal infilled with ferroelectric $BaTiO_3$. Appl Phys Lett 78(5):661–663. doi:10.1063/1.1344574
30. Leonard SW, Mondia JP, van Driel HM, Toader O, John S, Busch K, Birner A, Gosele U, Lehmann V (2000) Tunable two-dimensional photonic crystals using liquid-crystal infiltration. Phys Rev B: Condens Matter Mater Phys 61(4):R2389–R2392. doi:10.1103/PhysRevB.61.R2389
31. Kang D, Maclennan JE, Clark NA, Zakhidov AA, Baughman RH (2001) Electro-optic behavior of liquid-crystal-filled silica opal photonic crystals: effect of liquid-crystal alignment. Phys Rev Lett 86(18):4052–4055. doi:10.1103/PhysRevLett.86.4052
32. Mach P, Wiltzius P, Megens M, Weitz DA, Lin KH, Lubensky TC, Yodh AG (2002) Switchable Bragg diffraction from liquid crystal in colloid-templated structures. Europhys Lett 58(5):679–685. doi:10.1209/epl/i2002-00403-3
33. Gu ZZ, Fujishima A, Sato O (2000) Photochemically tunable colloidal crystals. J Am Chem Soc 122(49):12387–12388. doi:10.1021/Ja005595c
34. Sumioka K, Kayashima H, Tsutsui T (2002) Tuning the optical properties of inverse opal photonic crystals by deformation. Adv Mater 14(18):1284–1286. doi:10.1002/1521-4095(20020916)14:18<1284:Aid-Adma1284>3.0.Co;2-1
35. Lumsdon SO, Kaler EW, Williams JP, Velev OD (2003) Dielectrophoretic assembly of oriented and switchable two-dimensional photonic crystals. Appl Phys Lett 82(6):949–951. doi:10.1063/1.1541114
36. Fleischhaker F, Arsenault AC, Kitaev V, Peiris FC, von Freymann G, Manners I, Zentel R, Ozin GA (2005) Photochemically and thermally tunable planar defects in colloidal photonic crystals. J Am Chem Soc 127(26):9318–9319. doi:10.1021/ja0521573

37. Xia JQ, Ying YR, Foulger SH (2005) Electric-field-induced rejection wavelength tuning of photonic bandgap composites. Adv Mater 17(20):2463–2467. doi:10.1002/adma.200501166
38. Jeong U, Xia Y (2005) Photonic crystals with thermally switchable stop bands fabricated from Se@Ag2Se spherical colloids. Angew Chem Int Ed 44(20):3099–3103. doi:10.1002/anie.200462906
39. Maurer MK, Lednev IK, Asher SA (2005) Photoswitchable spirobenzopyran-based photochemically controlled photonic crystals. Adv Funct Mater 15(9):1401–1406. doi:10.1002/adfm.200400070
40. Barry RA, Wiltzius P (2006) Humidity-sensing inverse opal hydrogels. Langmuir 22 (3):1369–1374. doi:10.1021/la0519094
41. Yetisen AK, Naydenova I, Vasconcellos FC, Blyth J, Lowe CR (2014) Holographic sensors: three-dimensional analyte-sensitive nanostructures and their applications. Chem Rev 114 (20):10654–10696. doi:10.1021/cr500116a
42. Bjelkhagen HI (1995) Silver-halide recording materials for holography and their processing, 2nd edn. Springer, Heidelberg
43. Saxby G (2004) Practical holography, 3rd edn. Institute of Physics Publishing, London
44. Toal V (2011) Introduction to holography. CRC Press, Boca Raton
45. Bjelkhagen H, Brotherton-Ratcliffe D (2013) Ultra-realistic imaging: advanced techniques in analogue and digital colour holography. Taylor & Francis, Boca Raton
46. Montelongo Y, Tenorio-Pearl JO, Williams C, Zhang S, Milne WI, Wilkinson TD (2014) Plasmonic nanoparticle scattering for color holograms. Proc Natl Acad Sci USA 111 (35):12679–12683. doi:10.1073/pnas.1405262111
47. Maxwell JC (1865) A dynamical theory of the electromagnetic field. Philos Trans R Soc London 155:459–512. doi:10.1098/rstl.1865.0008
48. Zenker W (1868) Lehrbuch der Photochromie (textbook on photochromism). F. Viewag und Suhn, Berlin
49. Guther R (1999) The Berlin scientist and educator Wilhelm Zenker (1829–1899) and the principle of color selection. P Soc Photo-Opt Ins 3738:20–29
50. Hertz H (1893) Electric waves: being researches on the propagation of electric action with finite velocity through space. Macmillan Publishers, London
51. Wiener O (1890) Stehende Lichtwellen und die Schwingungsrichtung polarisirten Lichtes. Ann Phys (Berlin, Ger) 276 (6):203–243. doi:10.1002/andp.18902760603
52. Lippmann G (1894) Sur la Theorie de la Photographie des Couleurs Simples et Composees par la Methode Interferentielle. J Phys 3:97–107
53. Bjelkhagen HI (1997) Lippman photographs recorded in DuPont color photopolymer material, practical holography XI and holographic materials III, vol 3011. SPIE, San Jose
54. Bragg WL (1912) The diffraction of short electromagnetic waves by a crystal. Proc Cambridge Philos Soc 17:43
55. Wolfke M (1920) Über die Möglichkeit der optischen Abbildung von Molekulargittern. Physik Z 21:495–497
56. Gabor D (1948) A new microscopic principle. Nature 161(4098):777–778
57. Gabor D (1949) Microscopy by reconstructed wave-fronts. Proc R Soc A 197(1051):454–487. doi:10.1098/rspa.1949.0075
58. Einstein A (1917) Zur Quantentheorie der Strahlung (On the quantum theory of radiation). Physik Z 18:121–128
59. Gould RG (1959) The LASER, light amplification by stimulated emission of radiation. In: Franken PA, Sands RH (eds) The Ann Arbor conference on optical pumping, Ann Arbor, University of Michigan, p 128
60. Maiman TH (1960) Stimulated optical radiation in ruby. Nature 187(4736):493–494
61. Denisyuk YN (1962) On the reflection of optical properties of an object in a wave field of light scattered by it. Dokl Akad Nauk SSSR 144(6):1275–1278
62. Leith EN, Upatnieks J (1962) Reconstructed wavefronts and communication theory. J Opt Soc Am 52(10):1123–1128. doi:10.1364/JOSA.52.001123
63. Hariharan P (2010) Basics of interferometry. Academic Press, San Diego

64. Benton SA, Bove VM (2007) In-line "Denisyuk" reflection holography. In: Holographic imaging. Wiley, Hoboken, p 173. doi:10.1002/9780470224137.ch16
65. Kubota T (1988) Cross-Sectional view of Lippman hologram gratings. Appl Opt 27 (21):4358–4360. doi:10.1364/AO.27.004358
66. Blyth J (1979) "Pseudoscopic" moldmaking handy trick for Denisyuk holographers. Holosphere 8:5
67. Hariharan P (1980) Pseudocolour images with volume reflection holograms. Opt Commun 35(1):42–44. doi:10.1016/0030-4018(80)90356-9
68. Kaufman JA (1983) Previsualization and pseudo-color image plane reflection holograms. In: Proceeding of international symposium on display holography, Lake Forest College, IL, pp 195–207
69. Moore L (1983) Pseudo-color reflection holography. In: Proceeding of international symposium on display holography, Lake Forest College, IL, p 163
70. Wuest DR, Lakes RS (1991) Color control in reflection holograms by humidity. Appl Opt 30 (17):2363–2367. doi:10.1364/AO.30.002363
71. Walker JL (1987) In situ color control for reflection holography. M.S. Dissertation, MIT, Cambridge, U.S.
72. Walker JL, Benton SA (1989) In-situ swelling for holographic color control. In: Benton SA (ed) Practical holography III, Los Angeles, CA, SPIE, p 192
73. Spooncer RC, Al-Ramadhan FAS, Jones BE (1992) A humidity sensor using a wavelength-dependent holographic filter with fibre optic links. Int J Optoelectron 7(3):449–452
74. Lowe CR, Millington RB, Blyth J, Mayes AG (1995) Hologram used as a sensor. WO Patent Application 1995026499 A1
75. Blyth J, Millington RB, Mayes AG, Frears ER, Lowe CR (1996) Holographic sensor for water in solvents. Anal Chem 68(7):1089–1094. doi:10.1021/ac9509115
76. Millington RB, Mayes AG, Blyth J, Lowe CR (1996) A hologram biosensor for proteases. Sens Actuators B 33(1–3):55–59. doi:10.1016/0925-4005(96)01835-7
77. Postnikov VA, Kraiskii AV, Sergienko VI (2013) Holographic sensors for detection of components in water solutions. In: Mihaylova E (ed) Holography—basic principles and contemporary applications. InTech, Rijeka, p 103. doi:10.5772/53564
78. Mihaylova E, Cody D, Naydenova I, Martin S, Toal V (2013) Research on holographic sensors and novel photopolymers at the centre for industrial and engineering optics. In: Mihaylova E (ed) Holography—basic principles and contemporary applications. InTech, Rijeka, p 89. doi:10.5772/56061
79. Collier RJ, Burckhardt CB, Lin LH (1971) Optical holography. Academic Press, New York
80. Naydenova I, Jallapuram R, Martin S, Toal V (2011) Holographic humidity sensors. In: Okada CT (ed) Humidity sensors: types nanomaterials and environmental monitoring. Nova Science Publishers, Hauppauge, pp 117–142
81. Naydenova I, Jallapuram R, Toal V, Martin S (2009) Characterisation of the humidity and temperature responses of a reflection hologram recorded in acrylamide-based photopolymer. Sens Actuators B 139(1):35–38. doi:10.1016/j.snb.2008.08.020
82. Tsangarides CP (2013) Tuneable photonic crystal-based sensor using silver nanoparticles. MRes in photonic systems development dissertation, University of Cambridge, Cambridge
83. Tsangarides CP, Yetisen AK, da Cruz Vasconcellos F, Montelongo Y, Qasim MM, Wilkinson TD, Lowe CR, Butt H (2014) Computational modelling and characterisation of nanoparticle-based tuneable photonic crystal sensors. RSC Adv 4 (21):10454–10461. doi:10.1039/C3RA47984F
84. Yetisen AK, Butt H, da Cruz Vasconcellos F, Montelongo Y, Davidson CAB, Blyth J, Chan L, Carmody JB, Vignolini S, Steiner U, Baumberg JJ, Wilkinson TD, Lowe CR (2014) Light-directed writing of chemically tunable narrow-band holographic sensors. Adv Opt Mater 2(3):250–254. doi:10.1002/adom.201300375
85. Yetisen AK, Montelongo Y, da Cruz Vasconcellos F, Martinez-Hurtado JL, Neupane S, Butt H, Qasim MM, Blyth J, Burling K, Carmody JB, Evans M, Wilkinson TD, Kubota LT,

Monteiro MJ, Lowe CR (2014) Reusable, robust, and accurate laser-generated photonic nanosensor. Nano Lett 14(6):3587–3593. doi:10.1021/nl5012504
86. Yetisen AK, Montelongo Y, Qasim MM, Butt H, Wilkinson TD, Monteiro MJ, Lowe CR, Yun SH (2014) Nanocrystal Bragg grating sensor for colorimetric detection of metal ions (under review)
87. Yetisen AK, Qasim MM, Nosheen S, Wilkinson TD, Lowe CR (2014) Pulsed laser writing of holographic nanosensors. J Mater Chem C 2(18):3569–3576. doi:10.1039/C3tc32507e
88. John S (1987) Strong localization of photons in certain disordered dielectric superlattices. Phys Rev Lett 58(23):2486–2489. doi:10.1103/PhysRevLett.58.2486
89. Yablonovitch E (1987) Inhibited spontaneous emission in solid-state physics and electronics. Phys Rev Lett 58(20):2059–2062. doi:10.1103/PhysRevLett.58.2059
90. Mathger LM, Land MF, Siebeck UE, Marshall NJ (2003) Rapid colour changes in multilayer reflecting stripes in the paradise whiptail, Pentapodus paradiseus. J Exp Biol 206 (20):3607–3613. doi:10.1242/Jeb.00599
91. Cong HL, Yu B, Zhao XS (2011) Imitation of variable structural color in Paracheirodon innesi using colloidal crystal films. Opt Express 19(13):12799–12808. doi:10.1364/OE.19.012799
92. Crookes WJ, Ding LL, Huang QL, Kimbell JR, Horwitz J, McFall-Ngai MJ (2004) Reflectins: the unusual proteins of squid reflective tissues. Science 303(5655):235–238. doi:10.1126/science.1091288
93. Liu F, Dong BQ, Liu XH, Zheng YM, Zi J (2009) Structural color change in longhorn beetles Tmesisternus isabellae. Opt Express 17(18):16183–16191. doi:10.1364/OE.17.016183
94. Joannopoulos JD, Johnson SG, Winn JN, Meade RD (2011) Photonic crystals: molding the flow of light, 2nd edn. Princeton University Press, Princeton
95. Zimmerman WBJ (2006) Multiphysics modelling with finite element methods. World Scientific Publishing Company Incorporated, Singapore
96. Tokarev I, Minko S (2012) Tunable plasmonic nanostructures from noble metal nanoparticles and stimuli-responsive polymers. Soft Matter 8(22):5980–5987. doi:10.1039/C2sm25069a
97. Zhang XY, Hu A, Zhang T, Lei W, Xue XJ, Zhou Y, Duley WW (2011) Self-assembly of large-scale and ultrathin silver nanoplate films with tunable plasmon resonance properties. ACS Nano 5(11):9082–9092. doi:10.1021/nn203336m
98. Blyth J, Millington RB, Mayes AG, Lowe CR (1999) A diffusion method for making silver bromide based holographic recording material. Imaging Sci J 47(2):87–91
99. Deng S, Yetisen AK, Jiang K, Butt H (2014) Computational modelling of a graphene Fresnel lens on different substrates. RSC Adv 4(57):30050–30058. doi:10.1039/C4ra03991b
100. Kong X-T, Butt H, Yetisen AK, Kangwanwatana C, Montelongo Y, Deng S, Cruz Vasconcellos FC, Qasim MM, Wilkinson TD, Dai Q (2014) Enhanced reflection from inverse tapered nanocone arrays. Appl Phys Lett 105(5):053108. doi:10.1063/1.4892580
101. Vasconcellos FD, Yetisen AK, Montelongo Y, Butt H, Grigore A, Davidson CAB, Blyth J, Monteiro MJ, Wilkinson TD, Lowe CR (2014) Printable surface holograms via laser ablation. ACS Photonics 1(6):489–495. doi:10.1021/Ph400149m
102. Yetisen AK, Akram MS, Lowe CR (2013) Paper-based microfluidic point-of-care diagnostic devices. Lab Chip 13(12):2210–2251. doi:10.1039/c3lc50169h
103. Volpatti LR, Yetisen AK (2014) Commercialization of microfluidic devices. Trends Biotechnol 32(7):347–350. doi:10.1016/j.tibtech.2014.04.010
104. Yetisen AK, Volpatti LR (2014) Patent protection and licensing in microfluidics. Lab Chip 14(13):2217–2225. doi:10.1039/c4lc00399c
105. Akram MS, Daly R, Vasconcellos FC, Yetisen AK, Hutchings I, Hall EAH (2015) Applications of paper-based diagnostics. In: Castillo-Leon J, Svendsen WE (eds) Lab-on-a-chip devices and micro-total analysis systems. Springer, Berlin. doi:10.1007/978-3-319-08687-3_7
106. Yetisen AK, Jiang L, Cooper JR, Qin Y, Palanivelu R, Zohar Y (2011) A microsystem-based assay for studying pollen tube guidance in plant reproduction. J Micromech Microeng 21(5):054018. doi:10.1088/0960-1317/21/5/054018

107. Farandos NM, Yetisen AK, Monteiro MJ, Lowe CR, Yun SH (2014) Contact lens sensors in ocular diagnostics. Adv Health Mater. doi:10.1002/adhm.201400504
108. Yetisen AK, Martinez-Hurtado JL, da Cruz Vasconcellos F, Simsekler MC, Akram MS, Lowe CR (2014) The regulation of mobile medical applications. Lab Chip 14(5):833–840. doi:10.1039/c3lc51235e
109. Yetisen AK, Martinez-Hurtado JL, Garcia-Melendrez A, Vasconcellos FC, Lowe CR (2014) A smartphone algorithm with inter-phone repeatability for the analysis of colorimetric tests. Sens Actuators B 196:156–160. doi:10.1016/j.snb.2014.01.077

http://www.springer.com/978-3-319-13583-0

Holographic Sensors

Yetisen, A.K.

2015, XVIII, 162 p. 72 illus., 55 illus. in color., Hardcover
ISBN: 978-3-319-13583-0